Nanoscale simple-fluid behavior under steady shear

Xin Yong and Lucy T. Zhang*

Department of Mechanical, Aerospace & Nuclear Engineering, Rensselaer Polytechnic Institute, Troy, New York 12180, USA

(Received 17 January 2012; revised manuscript received 18 April 2012; published 9 May 2012)

In this study, we use two nonequilibrium molecular dynamics algorithms, boundary-driven shear and homogeneous shear, to explore the rheology and flow properties of a simple fluid undergoing steady simple shear. The two distinct algorithms are designed to elucidate the influences of nanoscale confinement. The results of rheological material functions, i.e., viscosity and normal pressure differences, show consistent Newtonian behaviors at low shear rates from both systems. The comparison validates that confinements of the order of 10 nm are not strong enough to deviate the simple fluid behaviors from the continuum hydrodynamics. The non-Newtonian phenomena of the simple fluid are further investigated by the homogeneous shear simulations with much higher shear rates. We observe the "string phase" at high shear rates by applying both profile-biased and profile-unbiased thermostats. Contrary to other findings where the string phase is found to be an artifact of the thermostats, we perform a thorough analysis of the fluid microstructures formed due to shear, which shows that it is possible to have a string phase and second shear thinning for dense simple fluids.

DOI: 10.1103/PhysRevE.85.051202 PACS number(s): 66.20.−d, 47.11.Mn, 83.60.−a, 47.61.−k

I. INTRODUCTION

Understanding shear rheology of dense fluids is of great importance for many fluid mechanics and chemical engineering applications. A low shear viscosity is generally desired to minimize the pumping cost and to increase the rate of mass transfer in processes such as chemical reactions and purifications. For other applications such as lubrication, a higher viscosity may be favorable. Shear-induced structural orderings and phase transitions are also of fundamental and technological interest. These rheological phenomena may involve a large variety of unexpected fluid behaviors. The study of these subjects can be extremely complex at the continuum scale and become even harder at the microscale and nanoscale. Growing interest in miniaturized designs of micro- and nanofluidic systems and devices eagerly demands a comprehensive understanding of the rheology of fluids in microscale and nanoscale confined geometries, e.g., nanochannel flows or shearing a thin film [1–3]. Highly confined nanochambers or channels manifest surface effects and finite-sized bulk effects, which could lead to fluid properties and behaviors significantly different from those at the macroscale [4].

To facilitate the understanding of shear rheology, numerous theoretical, experimental, and computational studies are focused on constructing correlations between the rheology and the microstructures for various fluids. In complex fluids such as colloidal suspensions and polymer solutions under a steady shear flow, both shear thinning and shear thickening were observed, along with different microstructures formed in the fluid [5–9]. These non-Newtonian behaviors, e.g., shear thinning, not only exist in complex fluids, but also are observed in simple fluids under certain conditions [10]. More than 100 years ago, Maxwell believed that all fluids have non-Newtonian properties. The reason that a simple fluid shows Newtonian behaviors is that its characteristic time corresponding to non-Newtonian features (i.e., Maxwell relaxation time) is too short to be observed by the available analysis techniques. However, numerical simulations provide an effective way to investigate these non-Newtonian phenomena in simple fluids. One of the pioneers of this work is Erpenbeck [11], who observed shear thinning in a hard-sphere fluid at moderate shear rates (approximate order of 0.1 reduced unit τ^{-1}) and an exotic "string phase" at high shear rates (approximate order of 1), where particles are arranged in strings in the flow direction with hexagonal symmetry in the plane normal to the flow direction. Most studies using nonequilibrium molecular dynamics (NEMD) or nonequilibrium Brownian dynamics have reported systematic and strong ordering in simple fluids undergoing either steady [12–15] or oscillatory [16,17] shear flows when the shear rates are high. On the other hand, several groups have argued that the ordering in steady shear is caused artificially by the thermostat algorithms [18–21]. They, instead, showed amorphous particle distributions and observed shear thickening.

To obtain rheological material functions such as shear viscosity and normal pressure differences, NEMD provides the ability to compute transport coefficients over a wide range of shear rates. There are two popular NEMD algorithms to generate a steady shear flow. One is boundary-driven shear [Fig. 1(a)], where the simulation mimics realistic interactions between the walls and the fluid and shows the steady state of the closed system. Boundary-driven shear generates a shear flow in a physical way by moving either one or both of the walls. The other is homogeneous shear [Fig. 1(b)], which ignores surface effects by only simulating the fluid ensemble and focuses more on the "bulk" properties of the fluid under shear. Among homogeneous shear methods, SLLOD and its related methods involving Lees-Edwards boundary conditions are perhaps better known [22,23]. These methods specify a shear field through a fictitious force term in the equations of motion and manipulates the simulation boundaries to preserve the flow. Liem *et al.* [24] showed that these two classes of methods gave similar results for key thermodynamic properties at sufficiently moderate shear rates. For both of these NEMD algorithms, the material functions are measured via appropriate components of the pressure tensor.

*zhanglucy@rpi.edu

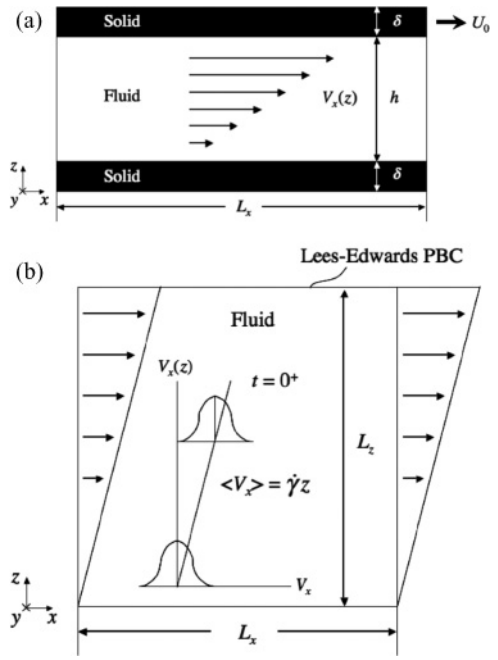

FIG. 1. Schematics of (a) boundary-driven shear and (b) homogeneous shear.

The objectives of this study are twofold. (i) The first goal is to perform rheological studies of a simple fluid at the nanoscale using boundary-driven shear and homogeneous shear. The flow velocity profiles and rheological quantities for both systems when they are under low shear rates (approximate order of 0.01 and smaller) are compared. The results are expected to be similar at low shear rates since the confinement in this study is not strong enough to cause the breakdown of bulk hydrodynamics (usually ∼1–2 nm) [3,4]. (ii) The second objective is to obtain the rheological quantities at high shear rates using homogeneous shear and correlate them with microstructural changes in the fluid. The corresponding non-Newtoninan behaviors are examined. To prevent the appearance of artifacts induced from the thermostats, appropriate thermostats are carefully applied in order to reduce viscous heating and allow the system to reach steady state without imposing a bias onto the system.

The outline of the paper is as follows: the details of the simulation models, system geometries, and thermostats to be used are presented in Sec. II. They are followed by the Results and Discussion in Sec. III. In this section, we closely examine the surface effects by comparing the fluid behaviors of the two NEMD systems. Non-Newtonian behaviors such as shear thinning, second shear thinning, and microstructures in the fluid are analyzed. Their relationships with rheological material functions are also studied. Finally, conclusions are drawn in Sec. IV.

II. NUMERICAL MODELING AND SETUP

A. Material functions

Rheological material functions are functions characterizing the rheological behaviors of a fluid. They depend on the stress responses $\boldsymbol{\tau}$ of a material while undergoing shear and elongational flows. Material functions, in general, are functions of time and kinematic parameters, e.g., strain or strain rate, that correspond to the type of flow imposed on the material.

Shear viscosity η is the material function that is the most commonly sought after as a rheological quantity in a steady shear flow. It is the primary material property that distinguishes a non-Newtonian fluid from a Newtonian fluid. For a Newtonian fluid, the shear viscosity η is a constant that is independent of the shear rate $\dot{\gamma}$, whereas for a non-Newtonian fluid, η could be a function of the shear rate, $\eta = \eta(\dot{\gamma})$. Shear thinning and shear thickening are the two most common phenomena that are associated with varying viscosity in a non-Newtonian fluid. For steady simple shear flows, η is typically defined as the ratio of the steady-state shear stress to the shear rate $\dot{\gamma}$:

$$\eta(\dot{\gamma}) = \lim_{t\to\infty} \frac{\tau_{xz}(t)}{\dot{\gamma}} = -\lim_{t\to\infty} \frac{P_{xz}(t)}{\dot{\gamma}}. \quad (1)$$

As shown in the equation, the shear stress can also be related to the pressure tensor $\mathbf{P}$ in the fluid. The shear rate $\dot{\gamma}$ is a gradient of one component of the fluid velocity, say the x direction (flow direction), with respect to another direction, say the z direction (gradient direction), $\frac{\partial v_x}{\partial z}$. The corresponding shear stress τ_{xz} represents the collinear momentum flux j_{xz} of the x component of the momentum p_x transported in the z direction per given time per unit area.

Another two important rheological material functions are the normal pressure differences. They are defined as

$$p_- = \tfrac{1}{2}(P_{xx} - P_{zz}); \quad p_0 = \tfrac{1}{2}\left[P_{yy} - \tfrac{1}{2}(P_{xx} + P_{zz})\right]. \quad (2)$$

p_- is associated with the rotation of the distorted microstructure and p_0 reflects the nonlinear bulk deformation [25,26]. For a Newtonian fluid, both p_- and p_0 are expected to be 0. In macroscopic non-Newtonian fluids, these normal pressure differences are responsible for a wide variety of interesting phenomena such as the Weissenberg effect [27]. The nonzero values of these two normal pressure differences are the key quantities associated with a non-Newtonian fluid.

As we have shown, these three rheological material functions all involve the computation of the pressure tensor, $\mathbf{P}$. In molecular dynamics simulations, several methods have been used to calculate the pressure tensor. The popular zeroth-order approximation of the Irving-Kirkwood expression [28] (same as the virial expression) calculates the pressure tensor in the domain of interest as

$$P_{\alpha\beta} = \frac{1}{V}\left(\sum_i^N m_i v_{i\alpha} v_{i\beta} + \frac{1}{2}\sum_i^N \sum_{j\neq i}^N r_{ij\alpha} f_{ij\beta}\right). \quad (3)$$

α and β represent the directional indices. i and j are the atom indices. V is the volume of the domain of interest. m_i and $\mathbf{v}_i$ are the particle mass and velocity, respectively. $\mathbf{r}_{ij}$ and $\mathbf{f}_{ij}$ are the distance and force vectors between a pair of particles. The first term in Eq. (3) is the kinetic part and the second one is the virial part. Note that for shear flows, $\mathbf{v}_i$ is the *thermal* or *peculiar* velocity with respect to the streaming velocity of the flow. This approach to computing the pressure tensor can be used for both boundary-driven shear and homogeneous shear NEMD.

In boundary-driven shear, the existence of real solid walls provides an alternative way to compute P_{xz} directly from the shear forces of the fluid atoms exerted on the wall atoms, $\mathbf{F}$:

$$P_{xz} = \sum_{i}^{N_{\text{wall}}} \sum_{j}^{N_{\text{fluid}}} F_{ij}^{x}/A_z, \tag{4}$$

where F_{ij}^{x} is the x component of force exerted on atom i due to atom j. $A_z = L_x \times L_y$ is the area of the wall normal to the z direction. We employ the results of both methods in calculating the viscosity in boundary-driven shear simulations. Both methods are expected to yield the same statistical results at steady state, when the shear stress at the interface is the same as the internal fluid stress. For the normal pressure differences, only the Irving-Kirkwood expression is used since the diagonal components of the pressure tensor in Eq. (2) refer to fluid-fluid interactions.

B. Computational details

1. Molecular potential

In our molecular dynamics simulations of a simple fluid, only short-range pairwise interactions between atoms are considered such that all atoms are treated as Lennard-Jones (LJ) particles. The interactions are modeled using the LJ potential:

$$V_{ij}(r) = 4\varepsilon_{ij}\left[\left(\frac{\sigma_{ij}}{r}\right)^{12} - \left(\frac{\sigma_{ij}}{r}\right)^{6}\right], \tag{5}$$

where r is the distance between any two atoms; ε_{ij} and σ_{ij} define the characteristic energies and length scales of the potential, respectively. A cutoff radius $r_c = 3.0\ \sigma_{ff}$ for the LJ potential is applied to all interactions to reduce the computation time.

In homogeneous shear simulations, subscriptions i and j are the indices for any two fluid atoms. In boundary-driven shear simulations, these indices represent either fluid or wall atoms. Parameters for interactions between different atom types are calculated using the geometric mixing rules,

$$\varepsilon_{wf} = \sqrt{\varepsilon_{ww}\varepsilon_{ff}}, \quad \sigma_{wf} = \sqrt{\sigma_{ww}\sigma_{ff}}. \tag{6}$$

The mass, potential, and size of all the wall atoms are the same as the fluid atoms, which lead to a strong wall-fluid interaction $\varepsilon_{wf} = 1.0\ \varepsilon_{ff}$ that makes the walls very hydrophilic [29,30]. It is expected to yield no-slip conditions at a low wall shearing velocity. LJ reduced units are used in the simulations that are nondimensionalized with respect to the fluid parameters. All subscripts in the parameters are dropped henceforth when the parameters are used as units.

2. System setups

The boundary-driven shear model uses an orthogonal simulation cell. As shown in Fig. 1(a), x is the flow or the shearing velocity direction, z is the velocity gradient direction, and y is called the neutral or vorticity direction. Periodic boundary conditions are imposed in the x and y directions. The steady simple shear flow is generated by moving the upper wall at a uniform velocity U_0 along the positive x direction while keeping the lower wall stationary. This NEMD simulation mimics a realistic experimental setup. The atomic sites are on the [001] plane of an fcc lattice with a lattice constant of $1.01\ \sigma$. The two walls are rigid walls without thermal motion, where the forces on wall atoms are zeroed out in order to maintain a perfect lattice structure during the simulation. The purpose of imposing rigid walls is to simplify the analysis by decoupling the dynamics of the fluid flow from the thermal effects generated from the viscous heating in the fluid and the heat conduction at the fluid-solid contact. Each wall consists of 1800 atoms that form four layers. The wall has a thickness of $\delta = 1.51\ \sigma$ and the fluid is confined in a channel with height $h \approx 40\,\sigma$. The fluid slab contains 7614 fluid atoms and has a density of $\rho_f \approx 0.844\ \sigma^{-3}$. The density ratio between the wall and the fluid is $\rho_w/\rho_f = 4.62$, which produces a highly incommensurable interface. The entire simulation cell $L_x \times L_y \times L_z$ is about $15.13 \times 15.13 \times 44.88\ \sigma^3$.

In homogeneous shear simulations, we employ a nonorthogonal system with the deforming cube representation of the Lees-Edwards boundary conditions instead of the commonly used orthogonal coordinate system in the sliding brick representation. The images of the atoms are taken with respect to a skew coordinate system in which the z axis forms an angle of $\theta = \cot^{-1}(\dot{\gamma}t)$ from the x axis. Applying the Lees-Edwards boundary conditions alone is capable of producing a shear flow. However, the shear motion induced purely by these boundary conditions takes time to propagate to the interior of the system, typically at the speed of sound. To eliminate this time lag, a typical practice is to artificially superimpose a linear velocity profile at the start of the nonequilibrium simulation. We first let the system reach the equilibrium state and record the momentum of each particle $\mathbf{p}_i^0$. At the beginning of the nonequilibrium simulation, $t = 0$, we superimpose a linear velocity profile onto the particles in the equilibrated system by applying momentum $\mathbf{p}_i\ (t = 0) = \mathbf{p}_i^0 + \hat{\mathbf{i}} m_i \dot{\gamma} z_i\ (t = 0)$, where i is the particle index and $\hat{\mathbf{i}}$ denotes the unit vector in the x direction for the simple shear. We then let the system evolve by conventional Newtonian dynamics. Superimposing a profile immediately generates the shear flow, and the Lees-Edwards boundary conditions preserve the flow. The number of fluid atoms in homogeneous shear simulations ranges from 1728 to 62208. The size of the simulation cell ranges from $20.16 \times 20.16 \times 5.04\ \sigma^3$ to $120.94 \times 120.94 \times 5.04\ \sigma^3$. The different simulation sizes are necessary to obtain enough statistics for each of the thermostats used. The details are explained in the next section.

All simulations initially assign fluid atoms with random velocities according to the Gaussian distribution that is scaled to produce a desired temperature with a mean of 0.0. The equation of motion is integrated using the velocity-Verlet algorithm with a time step of $0.005\ \tau$ in the LAMMPS Molecular Dynamics Simulator [31], where $\tau = (m\sigma^2/\varepsilon)^{1/2}$ is the characteristic time of the LJ potential. However, the time step may be reduced to $0.0003\ \tau$ for homogeneous shear with very high shear rates. In all simulations, it takes 1×10^5 time steps for the system to first reach equilibrium. Boundary-driven shear simulations typically require another 1×10^6 steps to reach steady state once shearing starts. The production period is at least another 5×10^5 steps to obtain statistical averages for stress, fluid velocity, and density profiles. It may extend to 3×10^6 steps for low-wall-shearing-velocity simulations to achieve better statistics. Homogeneous shear simulations

require at least 5×10^5 steps to reach steady state after shearing, which is followed by 5×10^5 to 5×10^6 production steps.

3. Thermostats

As long as the system is off-equilibrium, there is viscous dissipation occurring. Since we intend to decouple the thermal effects from the dynamics of the fluid, a thermostat device is applied exclusively on fluid particles to enforce a uniform temperature everywhere in both boundary-driven shear and homogeneous shear simulations. A Nosé-Hoover chain (NHC) thermostat [32] is a time-reversible and deterministic thermostat generating a well-defined canonical ensemble. It can be easily coupled to the system equations as the following:

$$\begin{aligned}
\dot{\mathbf{r}}_i &= \frac{\mathbf{p}_i}{m_i}, \\
\dot{\mathbf{p}}_i &= \mathbf{F}_i - \left[\mathbf{p}_i - m_i \mathbf{u}_s\left(\mathbf{r}_i\right)\right] \frac{p_{\eta_1}}{Q_1}, \\
\dot{\eta}_i &= \frac{p_{\eta_i}}{Q_i}, \\
\dot{p}_{\eta_1} &= \left[\sum_{i=1}^{N} \frac{\left[\mathbf{p}_i - m_i \mathbf{u}_s\left(\mathbf{r}_i\right)\right]^2}{m_i} - N_f k_B T\right] - p_{\eta_1} \frac{p_{\eta_2}}{Q_2}, \\
\dot{p}_{\eta_j} &= \left(\frac{p_{\eta_{j-1}}^2}{Q_{j-1}} - k_B T\right) - p_{\eta_j} \frac{p_{\eta_{j+1}}}{Q_{j+1}}, \quad 1 < j < M, \\
\dot{p}_{\eta_M} &= \left(\frac{p_{\eta_{M-1}}^2}{Q_{M-1}} - k_B T\right).
\end{aligned} \tag{7}$$

Here, $\mathbf{r}_i$ and $\mathbf{p}_i$ are the particle position and momentum in the laboratory frame of reference, respectively. $\mathbf{F}_i$ is the total conservative force on particle i, M is the length of the thermostat chains, and Q_j, $1 \leqslant j \leqslant M$ are thermostat coupling coefficients. N_f is the number of degrees of freedom. $\mathbf{u}_s\left(\mathbf{r}\right)$ is an important variable, which is the instantaneous local streaming velocity of the shear flow. The determination of $\mathbf{u}_s$ is not a trivial procedure because an incorrect evaluation could cause a thermostat to generate unphysical behaviors on the particles.

Thermostats can be classified into profile biased-thermostats (PBTs) and profile-unbiased thermostats (PUTs) based on the specific definition of $\mathbf{u}_s$. For planar simple shear flows, if we assume $\mathbf{u}_s\left(\mathbf{r}\right) = (\dot{\gamma} \times z, 0, 0)$, the corresponding thermostat is referred to as a PBT. A PBT artificially maintains a linear velocity profile, and any deviation from the linear profile is interpreted as the thermal fluctuation and is inhibited by the thermostat. As pointed out by Evans and Morriss [18], a PBT could be a reasonable assumption for low shear rates. However, as the shear rate increases, the Reynolds number increases and it is possible that a secondary flow due to turbulence may develop. An attempt to restore the linear profile at high shear rates is considerably dubious; the PBT might distort the dynamics of the system and cause artificial shear thinning.

On the other hand, if the streaming velocity profile is not assigned *a priori* but computed locally via simulations, the thermostat is categorized as a PUT. In past decades, discussions of PUTs have prompted different ways to compute the instantaneous local streaming velocity. Two notable ways are (i) representing the streaming velocity by a finite Fourier series expansion and computing the Fourier coefficient [19,20,33] and (ii) computing the spatially averaged particle velocity within subdomains of a simulation cell [14,18,34–36]. Here, we choose to calculate the streaming velocity using the latter for its robustness and ease of implementation. The $\mathbf{u}_s$ of each subdomain is evaluated by averaging the velocity of the particles within it each time step. Similarly to the notation introduced by Evans *et al.* [33], the simulation cell is divided into subdomains: slabs for one-dimensional (1D) coordinate dependences, bins for 2D coordinate dependences, and bricks for 3D coordinate dependences. If an $(x \times z)$ PUT is assumed, the simulation cell is divided into slabs with thickness D_z in the z direction. If an $(xyz \times yz)$ PUT is assumed, slabs are further subdivided into bins along the y direction, which means that the streaming velocity has three (xyz) components and is a function of yz. An $(xyz \times xyz)$ PUT means that three Cartesian components of the instantaneous local streaming velocity are allowed to be functions of the coordinates (x, y and z), $\mathbf{u}_s\left(\mathbf{r}\right) = u_{sx}\left(x,y,z\right)\hat{\mathbf{i}} + u_{sy}\left(x,y,z\right)\hat{\mathbf{j}} + u_{sz}\left(x,y,z\right)\hat{\mathbf{k}}$. It is well known that a PBT might dissipate heat and inhibit the formation of secondary flows. A PUT could underestimate the temperature because the thermal velocity could be misidentified as the local streaming velocity while the particles remain unthermostated. To correctly distinguish the thermal and streaming parts of the total velocity, the subdomain dimensions, especially those of the directions with huge velocity gradients, e.g., the shear is imposed in the z direction in this case, have to be chosen with caution by the following criterion [34]:

$$\frac{\dot{\gamma} D_z}{v_{th}} \ll 1 \ll \rho V_{\mathrm{sd}}. \tag{8}$$

ρ is the prescribed average particle density. $V_{\mathrm{sd}} = D_x \times D_y \times D_z$ denotes the subdomain volume. $v_{th} = \sqrt{k_B T / \min\left(m_i\right)}$ is the highest characteristic thermal velocity among the particle species. This requirement means that the choices of D_x, D_y, and D_z should be large enough to provide a reliable statistic in each subdomain and small enough to ensure an accurate local description of the streaming velocity even at high shear rates. In our simulations, this usually results in hundreds of slabs in the z direction.

For boundary-driven shear, applying an NHC thermostat requires the choice of the auxiliary algorithm PBT or PUT. As a result of the possible slip appearing at the fluid-solid interface, it is impractical to apply a PBT by assuming an *a priori* linear velocity profile. Thus, the fluid temperature is controlled at $T = 1.1\ \varepsilon/k_B$ using a PUT by applying the thermostat at every time step with a relaxation time of $0.05\ \tau$. In homogeneous shear, $T = 1.1\ \varepsilon/k_B$ is fixed by an NHC thermostat with either the PBT or the PUT assumption. The relaxation time of the thermostat is much shorter compared to that of boundary-driven shear and is varied for each simulation.

III. RESULTS AND DISCUSSION

A. Boundary-driven shear simulations

In boundary-driven shear simulations, the fluid is confined between two solid walls. The bulk of the fluid has a high

surface-to-volume ratio, where the interface may have a significant impact on the dynamic and structural properties of the bulk fluid. Previous simulation studies [1,37–39] confirmed that a solid wall constrains the motion of fluid atoms in both directions, parallel and perpendicular to the wall.

1. Velocity profiles vs. shear rates

Moving the upper wall shears the fluid slab and creates a steady simple shear flow (or planar Couette flow), which ideally should demonstrate a linear velocity profile. The time-averaged fluid velocity profiles for shearing velocities of $U_0 = 1.0\ \sigma/\tau$ to $U_0 = 9.0\ \sigma/\tau$ are plotted in Fig. 2(a). When the shearing velocity is low, e.g., $U_0 = 1.0\ \sigma/\tau$, the velocity profiles are perfectly linear in the bulk fluid region away from the walls. The velocity profile has small nonlinearities adjacent to the walls, which correspond to large wall-induced fluid density oscillations. This linear trend is consistent with the expectation for a Newtonian fluid under steady simple shear. When the applied shearing velocity is higher, i.e., $U_0 = 3.0,\ 5.0,$ and $7.0\ \sigma/\tau$, their velocity profiles are no longer linear even in the bulk region. This nonlinearity is also observed in previous MD studies on simple fluids [39,40]. Figure 2(b) shows the deviations of these velocity profiles from a linear profile. In this shearing velocity range, the fluid still remains amorphous and homogeneous except near the interface.

The reason for this nonlinearity in the velocity profile is the temperature in the system. Even though we intend to disassociate the dynamic and structural behaviors from the thermal effect by enforcing a uniform fluid temperature, as the shear rate gets higher, the fluid temperature inside the system starts to deviate from the set temperature of $T = 1.1\ \varepsilon/k_B$. This has also been observed in other studies [24,40,41]. To examine how the fluid temperature alters as a result of the shearing, a local fluid temperature (kinetic temperature) as a function of z for each slab of the simulation cell is computed by using the kinetic energy:

$$k_B T(z^j) = \frac{m_i}{3N^j - 3} \sum_{i=1}^{N^j} [\mathbf{v}_i - \mathbf{u}_s(\mathbf{r}_i)]^2 , \qquad (9)$$

where $\mathbf{v}_i$ is the particle velocity, $\mathbf{u}_s$ is once again the local streaming velocity, and z^j and N^j are the center coordinate of the jth slab in the z direction and the number of fluid atoms in the jth slab, respectively. Three degrees of freedom are cautiously excluded when the local temperature is evaluated because it is already involved in the evaluation of the local streaming velocity [34]. Figure 3 shows the time-averaged temperature profiles of the bulk fluid for different wall shearing velocities U_0. It is evident that the fluid starts to heat up near the walls when U_0 exceeds $3.0\ \sigma/\tau$. The increases in the fluid temperature at both lower and upper interfaces have the same magnitude. The core reason for the heating-up is that the rate of local viscous heating becomes significant when high slip velocities emerge. Simultaneously, the temperature around the center plane along the channel height exhibits a significant drop. This is to "maintain" the averaged temperature as the set temperature because the feedback mechanism of the NHC thermostat is based on the average temperature of the entire fluid.

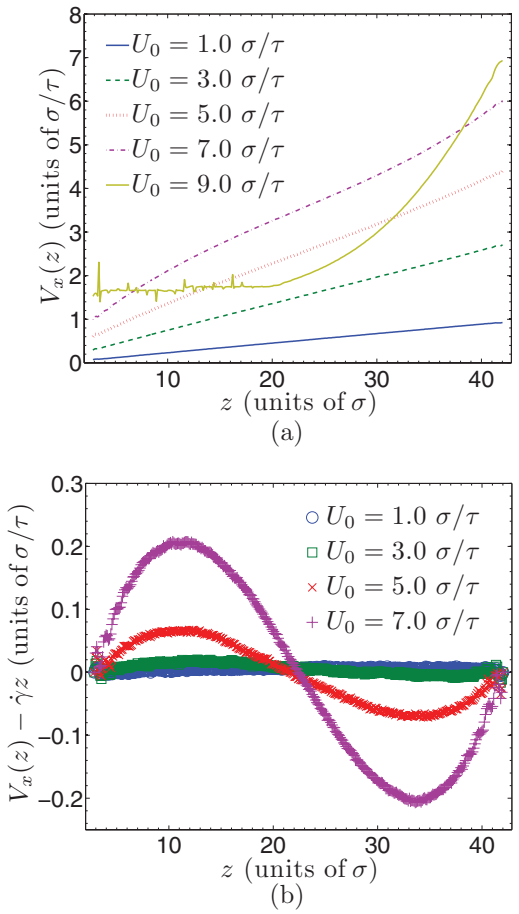

FIG. 2. (Color online) Time-averaged (a) velocity profiles and (b) deviations of velocity profiles from their corresponding linear forms along the z direction.

As the shearing velocity reaches $U_0 = 9.0\ \sigma/\tau$, the fluid forms a "layered" structure, referred to as the layer regime in the previous study [39]. The velocity profile has a segment with an approximately constant velocity, representing the collective translational movement of the layers. In the region where the fluid remains amorphous, the velocity still increases monotonically to match up with the upper wall shearing velocity. With the appearance of these ordered layers, the

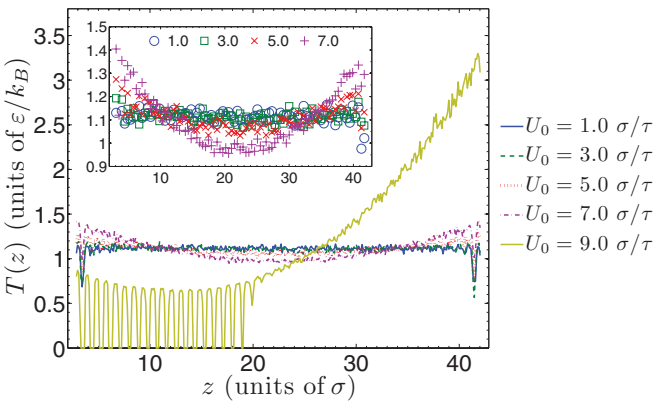

FIG. 3. (Color online) Time-averaged temperature profiles as a function of z for the tabulated shearing velocities.

temperature becomes totally nonuniform and asymmetric (see Fig. 3). The layer region has a temperature lower than the melting point corresponding to a solid-like structure. The emergence of the layered structure can be explained based on a thermal instability associated with the global nature of the NHC thermostat: at the start of the nonequilibrium process, the top wall starts moving from stationary. This large shearing force between the interacting fluid and the wall generates a large friction that results in substantial heating-up at the upper interface, which causes spontaneous symmetry breaking in the fluid system. The thermostat responds to that by significantly increasing the magnitude of the damping term, which reduces the thermal motion of other fluid atoms besides those at the upper interface. Once the local temperature of a certain portion of the fluid drops below the melting point, the fluid is going to nucleate and the spacial-modulated fluid atoms in the first fluid layer serve as nuclei. This mechanism explains why the formation of the layers always starts within the first fluid layer adjacent to the bottom wall and then propagates to the bulk.

2. *Material functions vs. shear rates*

Besides the velocity profiles examined above, the material functions can also provide a clear and quantitative representation of the nature in simple LJ fluids. In boundary-driven shear simulations, the viscosities at different fluid shear rates (up to the onset of the layer regime) are calculated from both the Irving-Kirkwood [Eq. (3)] and the shear force [Eq. (4)] approaches, shown in Fig. 4(a). When the layers appear, there is no physical definition of global shear viscosity in an inhomogeneous system. The fluid shear rate $\dot{\gamma}$ here is not directly proportional to the applied wall shearing velocity U_0 due to slippage at the interface. A high fluid shear rate cannot be produced due to the possible "overshear" of the fluid when a high wall shearing velocity is applied, which means that the fluid stays stagnant when the wall velocity is too high [42]. For a range of $U_0 = 0$ to $7.0\ \sigma/\tau$, a range of fluid shear rates from 0 to $0.12\ \tau^{-1}$ is produced. The approaches to calculating the pressure tensor yield very close viscosity results. Therefore, the fluid viscosity hereafter is expressed using the average of the two results. Consistent with previous MD results [40,43], the shear viscosity is found to be nearly constant at $\eta = 2.35 \pm 0.02\ \varepsilon\tau\sigma^{-3}$ and remains independent of the shear rate. This value is slightly lower than the value obtained later by our homogeneous shear and previous report [44]. We believe that the small deviation is caused by the surface effects of the nanoscale confinement. We conduct a series of simulations with different channel heights, and the result shows that the shear viscosities of the confined systems converge slowly to the one of the homogeneous shear system when the height is increased.

Two normal pressure differences, p_- and p_0, are also measured, shown in Fig. 4(b). Both are approximately zero at most of the simulated shear rates, up to $\dot{\gamma} = 0.1\ \tau^{-1}$, but become slightly nonzero at higher shear rates, $\dot{\gamma} > 0.1\ \tau^{-1}$. This is a clear indication of the fluid transitioning from Newtonian to non-Newtonian. However, if we trace back to the velocity profiles in Fig. 2, the nonlinearity starts to be significant at $U_0 = 3.0\,\sigma/\tau$, corresponding to a fluid shear rate of $\dot{\gamma} = 0.06\ \tau^{-1}$. At this shear rate, the fluid still has a constant

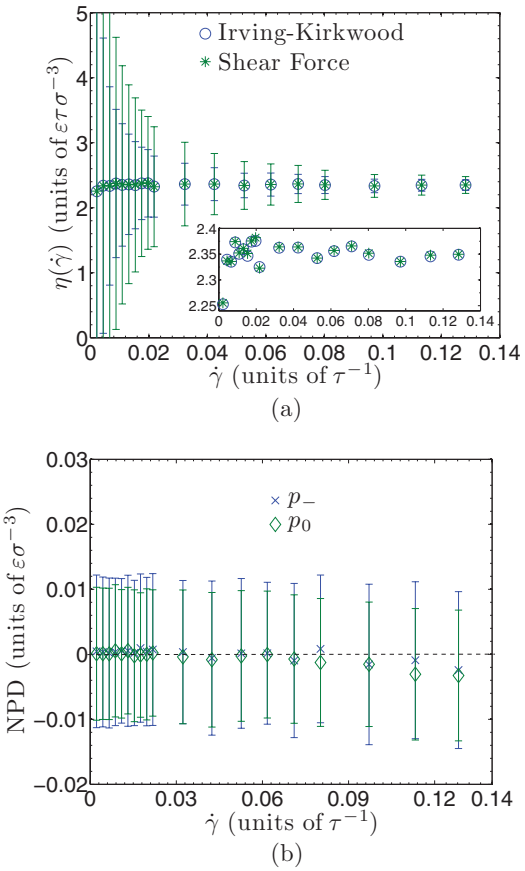

FIG. 4. (Color online) (a) Shear viscosity of the fluid in the channel using the Irving-Kirkwood expression (open circles) and the shear force expression (stars); (b) normal pressure differences p_- (crosses) and p_0 (open diamonds) at various shear rates.

viscosity and zero normal pressure differences. Therefore, based on the quantitative studies of material functions, it is clear that the nonlinearity in the velocity profile appears before the fluid transitions to non-Newtonian. This indicates that the nonlinearity is primarily induced by the viscous heating (from the temperature profile), rather than the fluid transitioning from Newtonian to non-Newtonian.

B. Homogeneous shear simulations

In homogeneous shear simulations, only the "bulk" of the fluid is modeled where the shear flow is driven by the initial perturbation with the Lees-Edwards periodic boundary conditions on the moving surface layers of the fluid atoms. The internal fluid is driven by its adjacent fluid in the shear flow. The fluid shear rate, therefore, can reach much higher values comparing to boundary-driven shear. Because the systems to be considered are at nanometer scales, the Reynolds numbers are maintained at low values even at extremely high shear rates. Therefore, homogeneous shear simulation provides a unique approach to study non-Newtonian behaviors at high shear rates without turbulence complicating the analysis. Similarly to the boundary-driven shear simulations, we first examine the non-Newtonian behaviors of simple fluids and thermostat influences by studying the velocity profiles of the system. Then the non-Newtonian behaviors are examined quantitatively

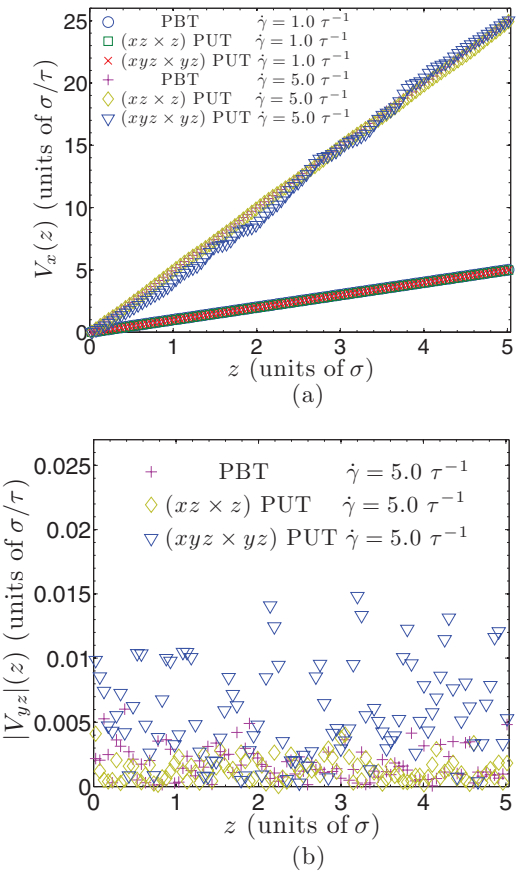

FIG. 5. (Color online) Time-averaged (a) fluid velocity profiles along the z direction and (b) magnitude of the disturbance in the y-z plane in systems with different thermostats at $\dot{\gamma} = 1.0\ \tau^{-1}$ and $\dot{\gamma} = 5.0\ \tau^{-1}$.

from the rheological material functions. The origin of these non-Newtonian phenomena are revealed by investigating the microstructure formed in the fluid.

1. Velocity profiles vs. shear rates

A range of shear rates $\dot{\gamma}$ from 0.001 to 10.0 τ^{-1} is imposed on the fluid. These shear rates are far beyond what the boundary-driven shear can produce but still have their corresponding Reynolds numbers to remain within laminar conditions. Here, we examine two representative shear rates, $\dot{\gamma} = 1.0\ \tau^{-1}$ and $\dot{\gamma} = 5.0\ \tau^{-1}$. The velocity profiles along the channel height direction z for these two shear rates are shown in Fig. 5(a). Three thermostats—a PBT, a 2D PUT ($xz \times z$), and a 3D PUT ($xyz \times yz$)—are used and their results are compared. At a relatively lower shear rate, e.g., $\dot{\gamma} = 1.0\ \tau^{-1}$, the V_x velocity profiles using the three thermostats all show a linear trend and yield nearly identical results. The linear profiles indicate that there is no significant secondary flow. The fluid is amorphous at this shear rate.

At a high shear rate, e.g., $\dot{\gamma} = 5.0\ \tau^{-1}$, the velocity profile in Fig. 5(a) shows that the ($xyz \times yz$) PUT yields substantially larger fluctuations when the disturbance in the y and z directions is not prohibited by the thermostat. Secondary flows in the y-z plane are observed. Figure 5(b) shows the magnitude of the disturbance in the y-z plane, which is computed as $|V_{yz}|(z) = \sqrt{V_y(z)^2 + V_z(z)^2}$. Meanwhile, the PBT prevents these behaviors and maintains a linear profile with no disturbance.

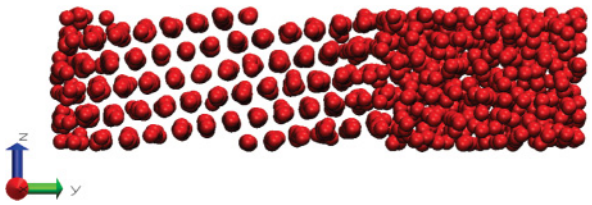

FIG. 6. (Color online) Snapshot of the string phase in the y-z plane view when $\dot{\gamma} = 5.0\ \tau^{-1}$.

At the high shear rate of $\dot{\gamma} = 5.0\ \tau^{-1}$, a string phase appears for all three thermostats. The string phase is where atoms form a hexagonal pattern in the y-z plane (i.e., vorticity-velocity gradient plane) as shown in Fig. 6. It is usually associated with significant instantaneous fluctuations and shear localization. They appear in the form of discontinuities in the velocity profile [45], as we also see in Fig. 5(a). Unlike the layered structure we found in the boundary-driven shear simulations, which is an artifact of the thermostat, the string phase appears most likely because of the non-Newtonian nature of the fluid. Unfortunately, this cannot be verified by experiments with the current available techniques. However, it is possible to draw similarities to the string phase with the observations from colloidal suspensions [7,46]. The following section on material functions analysis provides more information on the string phase.

2. Material functions vs. shear rates

The shear viscosity at shear rates from 0.001 to 10.0 τ^{-1} is first studied, shown in Fig. 7(a). The results for the three thermostats yield nearly the same result and show consistent shear rate dependency. Note that the quality of the data obtained at very low shear rates is quite poor, especially for the shear viscosity. It appears that the fluctuation at low shear rates creates a high noise-to-signal ratio, which makes it difficult to measure. The shear viscosity can be separated into three regions by two characteristic shear rates, the non-Newtonian transition shear rate $\dot{\gamma}_{nt}$ and the critical shear rate $\dot{\gamma}_{cr}$. The non-Newtonian transition shear rate $\dot{\gamma}_{nt}$ is located at $\dot{\gamma}_{nt} \approx 0.1\ \tau^{-1}$, which separates the viscosity from the constant (Newtonian) to the shear thinning (non-Newtonian) region. The shear-thinning region can be fitted well by the three-parameter Carreau model [47]. This transition shear rate has a magnitude that is consistent with the result we obtained for the boundary-driven shear. The critical shear rate $\dot{\gamma}_{cr}$ defines the transition from the shear thinning region to a third region which is separated by a sudden drop in the viscosity at $\dot{\gamma}_{cr} \approx 3.0\ \tau^{-1}$. The third region is normally called the second shear-thinning region because of the rapid decrease in the viscosity. The fluid remains amorphous until the shear rate reaches $\dot{\gamma}_{cr}$, and the string phase emerges along with the second shear thinning above $\dot{\gamma}_{cr}$. The viscosity drop associated with the string phase was analyzed in previous studies [13,48]. When the strings appear, the fluid particles are more widely spaced within a string than between the strings, which leads to a higher self-diffusion coefficient

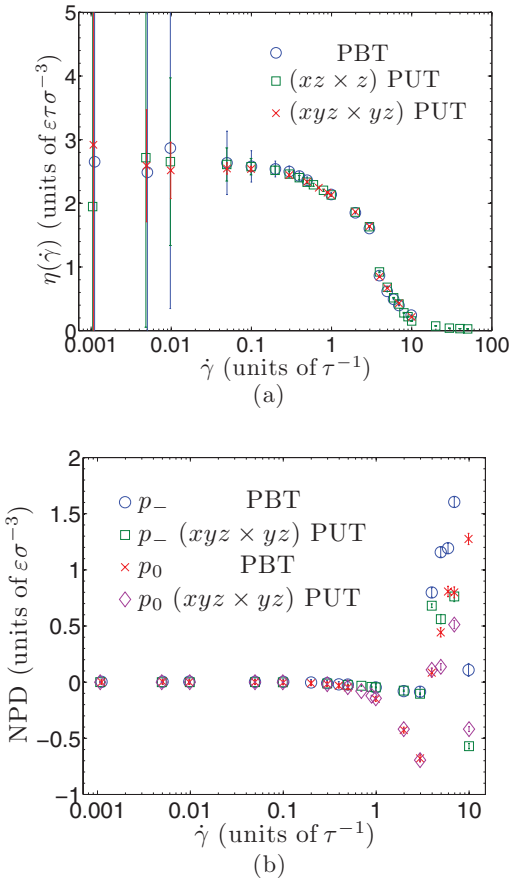

FIG. 7. (Color online) (a) Fluid viscosity and (b) normal pressure differences as functions of the shear rate with different thermostats.

component in the x direction. Consequently, the viscosity decreases.

The two normal pressure differences regarding the shear rates are shown in Fig. 7(b). At low shear rates, p_- and p_0 are approximately zero, which is associated with the constant viscosity, confirming that the atomistic fluid is Newtonian at low shear rates. In the shear thinning region, both normal pressure differences decrease monotonically until reaching $\dot{\gamma}_{\rm cr}$. For $\dot{\gamma} > \dot{\gamma}_{\rm cr}$, p_- and p_0 scatter without any obvious trend, which is related to the appearance of the string phase. In this range of shear rates, the string phase contains large fluctuations in flow properties and shear localization, therefore the normal pressure differences for different thermostats in the second shear thinning region are shown to be more sporadic.

Stability analysis and direct numerical simulations [49,50] showed that the linear velocity profile for simple shear flow is stable upon arbitrary infinitesimal perturbations for Re $<$ 125. For the systems in this work, the critical shear rate $\dot{\gamma}_{\rm cr} \approx 3.0\,\tau^{-1}$ corresponds to Re $\approx$ 9.8. Therefore, rheological behaviors, such as the viscosity and the normal pressure differences observed above, are truly due to the non-Newtonian nature of the simple fluid preventing the possible onset of turbulence.

The consistent non-Newtonian behaviors and the appearance of the string phase we observe for all three thermostats contradict other studies [18,51], where McWhirter showed that an $(xyz \times xyz)$ PUT prevents the onset of the string phase because large vortices exist in the y-z plane [51]. On the contrary, the PUT thermostats we have simulated still sustain the string phase as long as the spatial average of the particle velocity is statistically reliable.

A possible physical interpretation of the string phase is proposed in the following by analogy to colloidal suspensions. In a comprehensive discussion of colloidal suspensions [9,52], Foss *et al*. stated that the string phase forms in colloidal suspensions when there are repulsive forces among colloidal particles. The repulsive forces prevent particles from getting close enough for the buildup of short-range lubrication forces which disrupt any order that may form. For simple fluids, the absence of solvent means that there is no lubrication force to prevent the onset of the string phase and shear thinning continues. Thus, based on the similarities in the formation of the string phase, we believe that the string phase we observe is likely not an artifact and it is possible for the second shear thinning and the string phase to occur in simple fluids. To investigate whether the string phase is possibly a physical behavior induced by high shear rates, we further look into the pattern of the fluid structural change due to different shear rates.

3. *Shear-induced microstructures*

Shear-induced distortion of the fluid particle distribution is believed to be responsible for the non-Newtonian phenomenon in simple fluids [10]. The behavior is similar to that of colloidal suspensions [53]. To qualitatively investigate the structural change, the projections of the pair distribution function $g(\mathbf{r})$ on different planes are measured. The pair distribution function describes the distribution of distances between pairs of particles contained within the simulation cell. The projection of it on the x-y plane is defined as

$$g(x,y) = \frac{N(x,y,\Delta x,\Delta y)}{N_t \rho_{xy} A(x,y,\Delta x,\Delta y)}, \tag{10}$$

where $N(x,y,\Delta x,\Delta y)$ is the number of particles found in a square area $A(x,y,\Delta x,\Delta y)$ located at (x,y) with respect to the sampled center particle, N_t is the total number of particles within the simulation cell, and ρ_{xy} is the planar number density in the x-y plane. Other projections can be obtained in the same manner.

Figure 8 shows $g(\mathbf{r})$ projected onto three planes (x-z, y-z, and x-y) when the fluid is sheared at shear rates $\dot{\gamma} = 0.0$, 0.5, 2.0, and 5.0 τ^{-1}. The column "eqm" is a reference and shows the equilibrium particle distribution for the fluid at rest, i.e., $\dot{\gamma} = 0.0\ \tau^{-1}$. The intensity of the distribution corresponds to the probability of finding a particle in a given region and is measured by the darkness of the shading: the lighter the shading, the higher the probability. Since the fluid is isotropic at equilibrium, $g(\mathbf{r})$ has no directional dependence. The intensity pattern is radially symmetric in all three planes as expected. For a Newtonian flow regime where $\dot{\gamma} = 0.5$, the microstructure distortion is mainly limited in the x-z plane, i.e., the velocity-velocity gradient plane, where the circular pair distribution function becomes a biaxial ellipsoid with the long principal axis aligning with the extensional

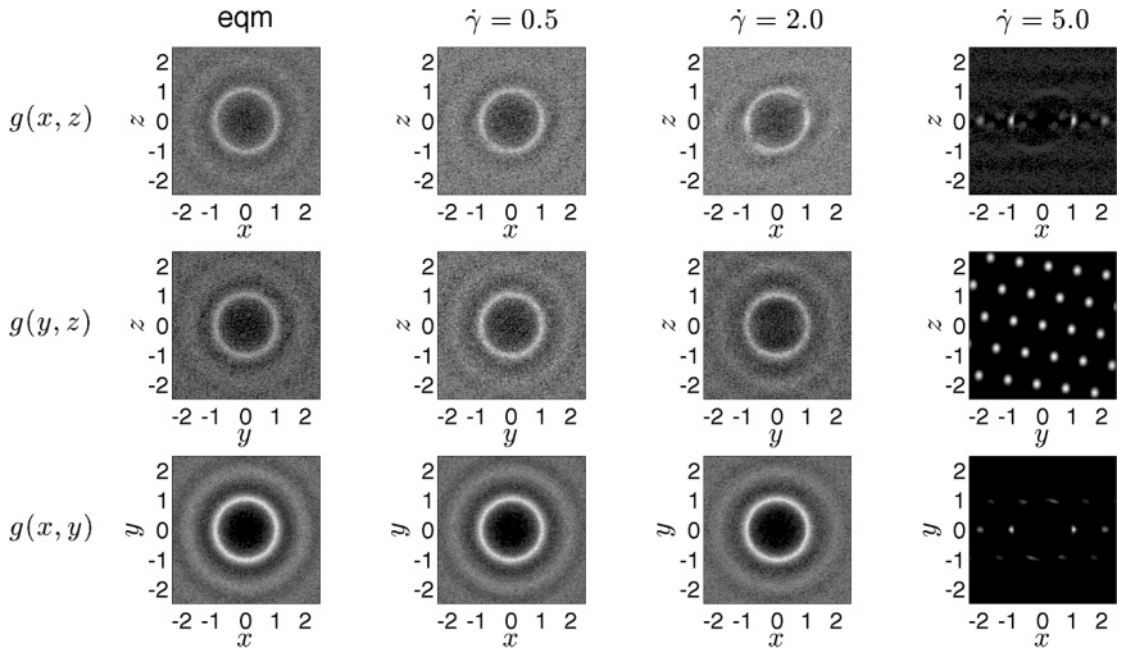

FIG. 8. Projections of the pair distribution function in all three planes at $\dot{\gamma} = 0$, 0.5, 2.0, and 5.0 τ^{-1}.

axes at $\pi/4$ and the short principal axis aligning with the compressive axes at $3\pi/4$. The intensity becomes higher along the compressive axes in the second and fourth quadrants. The projection of $g(\mathbf{r})$ on the y-z plane is still radially symmetric. When shear thinning occurs, e.g., $\dot{\gamma} = 2.0$, the deformation of $g(\mathbf{r})$ is so large that the long axis rotates away from the extensional axes in the x-z plane and a distortion is introduced even in the y-z plane. These microstructure distortions in fluid atoms closely relate to shear thinning with negative p_- and p_0. Based on these observations, shear thinning can be explained such that as the shear rate rises, shear stress increases correspondingly; the particles diffuse against the flow, trying to recover to their unstressed equilibrated distribution. The particle diffusion eventually can no longer keep up with the flow, the microstructure distortion saturates, and shear thinning starts. As the shear rate increases further, e.g., $\dot{\gamma} = 5.0$, an ordered structure for the string phase appears. A hexagonal pattern is clearly found in the y-z plane.

A PUT thermostat is used in this simulation. The system with a PBT yields a pair distribution function very similar to the one in the system with a PUT, which confirms that different thermostats do not influence the essential behaviors of the systems. This study shows that the formation of the string phase is possible due to the high shear rate, not the choice of thermostat.

IV. CONCLUSIONS

In this study, we simulated a simple fluid using two NEMD approaches: the boundary-driven shear and homogeneous shear algorithms. Our rheological results on the simple fluid validate that the confinement used in this work was not strong enough to deviate from the bulk hydrodynamics. At low shear rates, the simple fluid showed its Newtonian nature, e.g., a constant shear viscosity and zero normal pressure differences, consistently in the boundary-driven shear and homogeneous shear simulations. The nonlinearities of the velocity profiles in the bulk fluid region found in the boundary-driven shear simulations were due to the temperature variations caused by the interfacial friction generated at the surfaces. The layered structure formed in the fluid is also an artifact due to the thermostat.

The non-Newtonian behaviors of the simple fluid at high shear rates were further studied by homogeneous shear simulations. The PBT and PUT essentially yielded identical non-Newtonian phenomena when the NHC thermostat is applied. The minor differences between the PBT and the PUT were only revealed in the velocity profiles and small discrepancies in the material functions after the onset of the string phase. By relating shear thinning to the shear-induced fluid microstructure distortion and the particle pair distribution function, we discussed a rational hypothesis for the formation of the string phase. Our results suggest that the second shear thinning and the string phase are possibly physical behaviors due to high shear rates rather than purely thermostat artifacts for dense simple fluids. Taking into account the global and local natures of different thermostat algorithms may also be required for a better understanding of non-Newtonian behaviors of simple fluids at high shear rates.

ACKNOWLEDGMENTS

This work was partially supported by the NRC (Grant No. NRC-38-09-954) and the NSF (Grant No. CMMI-0928448). The authors wish to thank Dr. N. V. Priezjev for pertinent comments on this work. The computational work for this research was performed at the Rensselaer Polytechnic Institute Computational Center for Nanotechnology Innovations.

[1] P. A. Thompson and M. O. Robbins, Phys. Rev. A **41**, 6830 (1990).
[2] P. A. Thompson and M. O. Robbins, Science **250**, 792 (1990).
[3] A. Martini, Y. Liu, R. Snurr, and Q. Wang, Tribol. Lett. **21**, 217 (2006).
[4] L. Bocquet and E. Charlaix, Chem. Soc. Rev. **39**, 1073 (2010).
[5] M. C. Newstein, H. Wang, N. P. Balsara, and A. A. Lefebvre, J. Chem. Phys. **111**, 4827 (1999).
[6] B. Maranzano and N. Wagner, J. Chem. Phys. **117**, 10291 (2002).
[7] B. Ackerson, J. Rheol. **34**, 553 (1990).
[8] L. Chen, B. Ackerson, and C. Zukoski, J. Rheol. **38**, 193 (1994).
[9] J. F. Brady, Chem. Eng. Sci. **56**, 2921 (2001).
[10] D. J. Evans, H. Hanley, and S. Hess, Phys. Today **37**, 26 (1984).
[11] J. J. Erpenbeck, Phys. Rev. Lett. **52**, 1333 (1984).
[12] D. Heyes, G. P. Morriss, and D. J. Evans, J. Chem. Phys. **83**, 4760 (1985).
[13] D. Heyes, J. Chem. Soc. Faraday Trans. II **82**, 1365 (1986).
[14] W. Loose and S. Hess, Rheol. Acta **28**, 91 (1989).
[15] T. Yamada and S. Nosé, Phys. Rev. A **42**, 6282 (1990).
[16] W. Xue and G. Grest, Phys. Rev. Lett. **64**, 419 (1990).
[17] H. Komatsugawa and S. Nosé, J. Chem. Phys. **112**, 11058 (2000).
[18] D. J. Evans and G. P. Morriss, Phys. Rev. Lett. **56**, 2172 (1986).
[19] K. P. Travis, P. J. Daivis, and D. J. Evans, J. Chem. Phys. **103**, 10638 (1995).
[20] K. P. Travis, P. J. Daivis, and D. J. Evans, J. Chem. Phys. **105**, 3893 (1996).
[21] J. Delhommelle, J. Petravic, and D. J. Evans, Phys. Rev. E **68**, 031201 (2003).
[22] M. Allen and D. Tildesley, *Computer Simulation of Liquids* (Oxford University Press, New York,1987).
[23] D. J. Evans and G. P. Morriss, *Statistical Mechanics of Nonequilibrium Liquids* (Academic Press, London, New York,1990).
[24] S. Y. Liem, D. Brown, and J. H. Clarke, Phys. Rev. A **45**, 3706 (1992).
[25] S. Hess, Physica A **118**, 79 (1983).
[26] L. V. Woodcock, Chem. Phys. Lett. **111**, 455 (1984).
[27] F. A. Morrison, *Understanding Rheology* (Oxford University Press, New York, 2001).
[28] J. Irving and J. Kirkwood, J. Chem. Phys. **18**, 817 (1950).
[29] R. S. Voronov, D. V. Papavassiliou, and L. L. Lee, J. Chem. Phys. **124**, 204701 (2006).
[30] X. Yong and L. T. Zhang, Langmuir **25**, 5045 (2009).
[31] S. Plimpton, J. Comput. Phys. **117**, 1 (1995).
[32] G. J. Martyna and M. L. Klein, J. Chem. Phys. **97**, 2635 (1992).
[33] D. J. Evans, S. Cui, H. Hanley, and G. Straty, Phys. Rev. A **46**, 6731 (1992).
[34] W. Loose and G. Ciccotti, Phys. Rev. A **45**, 3859 (1992).
[35] P. Padilla and S. Toxvaerd, J. Chem. Phys. **103**, 716 (1995).
[36] K. Bagchi, S. Balasubramanian, C. Mundy, and M. Klein, J. Chem. Phys. **105**, 11183 (1996).
[37] J.-L. Barrat and L. Bocquet, Phys. Rev. Lett. **82**, 4671 (1999).
[38] N. V. Priezjev, Phys. Rev. E **75**, 051605 (2007).
[39] X. Yong and L. T. Zhang, Phys. Rev. E **82**, 056313 (2010).
[40] A. Niavarani and N. V. Priezjev, Phys. Rev. E **81**, 011606 (2010).
[41] A. Niavarani and N. V. Priezjev, Phys. Rev. E **77**, 041606 (2008).
[42] X. Yong and L. T. Zhang, Proc. Inst. Mech. Eng. Part N J. Nanoeng. Nanosyst. **224**, 19 (2010).
[43] P. A. Thompson and S. M. Troian, Nature **389**, 360 (1997).
[44] G. Galliéro, C. Boned, and A. Baylaucq, Ind. Eng. Chem. Res. **44**, 6963 (2005).
[45] R. Gray, S. Chynoweth, Y. Michopoulos, and G. Pawley, Europhy. Lett. **43**, 491 (1998).
[46] B. Ackerson and P. Pusey, Phys. Rev. Lett. **61**, 1033 (1988).
[47] C. M. Tenney and E. J. Maginn, J. Chem. Phys. **132**, 014103 (2010).
[48] J. McWhirter and G. Patey, J. Chem. Phys. **117**, 2747 (2002).
[49] M. Nagata, J. Fluid Mech. **217**, 519 (1990).
[50] A. Lundbladh and A. V. Johansson, J. Fluid Mech. **229**, 499 (1991).
[51] J. McWhirter, J. Chem. Phys. **118**, 2824 (2003).
[52] D. R. Foss and J. F. Brady, J. Fluid Mech. **407**, 167 (2000).
[53] J. Vermant and M. Solomon, J. Phys. Condens. Matter **17**, 187 (2005).